Eur. Phys. J. Plus (2019) **134**: 435
DOI 10.1140/epjp/i2019-12819-3

THE EUROPEAN PHYSICAL JOURNAL PLUS

Regular Article

Sensitivity comparison of surface plasmon resonance (SPR) and magneto-optic SPR biosensors

Conrad Rizal[1,2,a] and Vladimir Belotelov[3,4,b]

[1] Electrical Engineering & Computer Science, York University, 4700 Keele St, Toronto, ON, M3J 1P3, Canada
[2] Nanophotonics Laboratory, GEM Systems Inc., Markham, ON, L3R 5H6, Canada
[3] Lomonosov Moscow State University, Leninslie Gory, 1, bld.2, Moscow 119992, Russia
[4] Russian Quantum Center, Business-center, "Ural", Skolkovskoe shosse 45, Moscow 121353, Russia

Received: 10 March 2019
Published online: 10 September 2019

Abstract. Sensitivity of a biosensor is one of the most important parameters that determines its performance. It depends on many factors, such as excitation wavelength of incident optical radiation (λ), composition, type, and thickness of the ferromagnetic Co layer (t_{Co}), plasmonic Au, and high refractory metal, Ti, involved, and sensing/excitation configuration. In this paper, both the surface plasmon resonance (SPR at the magnetic field, $H = 0$) and magneto-optic SPR (MOSPR at H) sensitivity of the sensors have been theoretically calculated in the visible wavelength regime using air-helium media as probing samples in the *Kretschmann* configuration, and their performances are compared side by side. The calculated MOSPR sensitivity of 1.25×10^5%/RIU (refractive index unit) at $\lambda = 632.8$ nm is almost 12.5× larger as compared to the SPR sensitivity of 1.0×10^4%/RIU for the same geometry, excitation condition, and probing media. Likewise, the MOSPR sensitivity of 1.25×10^5%/RIU at $\lambda = 632.8$ nm is almost 10× larger as compared to the MOSPR sensitivity of 1.25×10^4%/RIU at $\lambda = 515$ nm for the same geometry and probing media. On decreasing the t_{Co}, the sensitivity of the MOSPR sensor is further increased by almost 3×, from 1.25×10^5%/RIU at $t_{\mathrm{Co}} = 8$ nm to 3.7×10^5%/RIU at $t_{\mathrm{Co}} = 4$ nm. The sensitivity can be further improved by additional optimization of the material used and sensor configuration employed for detection.

1 Introduction

Biosensing using magneto-optic surface plasmon resonance (MOSPR) is a relatively new method that carries significant promise to fundamental studies and technological applications [1,2]. The MOSPR-based sensing has also many advantages over the conventional SPR-based sensing [3]. For example, the sensors based on MOSPR require less number of sensing samples, are free from electromagnetic interferences, and demonstrate higher sensitivity and larger signal-to-noise ratio compared to the sensors based on SPR effects [4]. While in the SPR configuration, the excitation condition is determined by the optical radiation and surface plasmons generated at the interface between the metals and dielectric layers, in the MOSPR configuration, the excitation condition is determined by the magnetic activity in addition to the optical radiation and surface plasmons and these allow MOSPR sensors to be more robust in tuning and amplifying the output signal/response of the sensor [5–9].

Magneto-optical plasmonic Co/Au multilayers are of significant scientific importance due to their remarkable MOSPR properties in both visible and near IR-regimes [4–8]. At the specific excitation conditions (wavelength and incident angle) and the magnetic, H field applied in the transverse direction, the stimulated resonance oscillation of valence electrons dramatically reduces the reflected light intensity from the sensor surface and produce SPR. The resonance condition is influenced by the type and amount of the sensing material (air and helium, in this case) adsorbed onto the sensor surface, the direction of an applied H field, which is transverse in this case, and the sensor configuration employed.

[a] e-mail: crizal@yorku.ca
[b] e-mail: v.i.belotelov@ya.ru

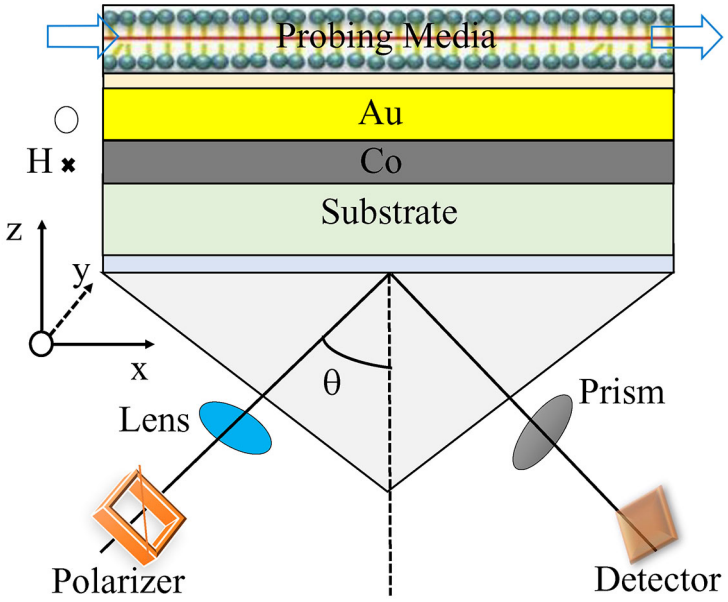

Fig. 1. Schematic of the SPR/MOSPR sensor in the *Kretschmann* configuration. The large arrows show the direction of the gas flow.

In the literature, three commonly used configurations for plasmon excitation exist. These include: i) *Kretschmann* [10], ii) *Otto* [11], and iii) grating [12] configurations. Out of all three configurations, this work reports on the *Kretschmann* configuration as it is comparatively accurate, easier to assemble, and test [13–22].

In this paper, the functionality of the MOSPR sensor is numerically demonstrated using Co and Au layer of 8 nm and 50 nm, respectively using three different excitation wavelengths, λ, as 515, 532, and 632.8 nm. Due to the excellent adhesion properties, a 2 nm thick Ti is also employed as a buffer layer. The theoretical model suggested that the sensitivity is significantly enhanced by an order when the operating λ is increased from 515 to 632.8 nm. The sensitivity is further improved when the 8 nm thickness of Co layer is replaced by 4 nm.

One of the important challenges of the existing biosensors is that no single sensing metrics are available to compare their performances. This paper presents new sensitivity models for direct comparision of the performance of SPR and MOSPR sensors in the visible regime [13].

2 Material and methods

Figure 1 shows schematics of the proposed SPR/MOSPR sensor configuration investigated in this study. The sensor configuration in the present case consists of thin metallic multilayer of Au and Co, directly placed on a glass substrate (BK-7) that is attached to the triangular prism shown here using an index matching liquid. The sensing media/probing samples consisted of air and helium, and they are kept in contact with the top most Au layer —the sensor surface, through a silicone channel/tube for the gas flow.

A 2 nm thick Ti is also used as an adhesion layer between the Co and glass substrate (not shown here). The permittivity of an index matching liquid (as shown by a thin layer between the prism and glass substrate) was also taken into account for calculation. The 50 nm Au layer also works as a capping layer in addition to the sensing layer. The top section of the sensor shows a channel (denoted by probing media) for passing probing gases to the sensor surface for detection. Unlike in most published works, in the present case, Co is placed towards the substrate side, as reported in our previous work [13].

Although a full insight into MOSPR sensor would require quantum mechanics considerations, it can also be described in terms of classical electromagnetic theory by considering wave reflection, transmission, and absorption for the multilayer medium. The *Kretschmann* configuration typically used for MOSPR studies has been analyzed here using transfer-matrix method and *COMSOL Multiphysics* in order to define the effect of external H field and excitation λ (in the visible regime) on SPR and sensitivity. Various optical and geometrical parameters of the sensor configurations are given in table 1.

There are many parameters that determine the resonance condition of the MOSPR configuration, such as wavelength of the incident light, λ incident angle, θ, thickness of the plasmonic/magnetic layers, the refractive indices of

Table 1. Optical and geometrical parameters of sensor configurations in the visible regime (λ = 515, 532 and 632.8 nm); $\delta n = (n_{\text{air}} - n_{\text{helium}})$. The ϵ_{mo} value inside small brackets is the magneto-optic constant for Co. The t denotes the layer thickness of metals in nanometer (nm).

Material	t (nm)	$\epsilon/(\epsilon_{mo})$ ($\lambda = 515$ nm)	$\epsilon/(\epsilon_{mo})$ ($\lambda = 532$ nm)	$\epsilon/(\epsilon_{mo})$ ($\lambda = 632.8$ nm)	Source
BK-7	1.3×10^6	2.3118	2.3088	2.2940	[15]
Ti	2	$-4.8562 + j15.849$	$-4.8562 + j15.849$	$-6.866 + j20.36$	[16]
Au	50	$-3.573 + j2.909$	$-4.856 + j15.85$	$-11.13 + j1.327$	[17]
Co	2	$-9.518 + j14.219$/ $(-0.50 + j0.0004)$	$-9.945 + j14.95$/ $(-0.52 + j0.00042)$	$-12.48 + j18.45$/ $(-0.65 + j0.0005)$	[18]
He	–	1.00006985	1.00006980	1.00006977	[19]
Air	–	1.000557	1.000556	1.0005530	[22]
δn	–	0.000487	0.000486	0.000483	[13]

the metals, prism, sensing media (dielectric media), and the orientation of the applied H field. Under the resonant condition, the incident angle is known as resonant angle, θ_{SPR}, and it is given as [13]

$$\theta_{\text{SPR}} = \sin^{-1}\left[\frac{1}{\sqrt{(\epsilon_p)}} \times \sqrt{\frac{(\epsilon_d \times \mu_d) \times (\epsilon_m \times \mu_m)}{(\epsilon_d \times \mu_d + \epsilon_m \times \mu_m)}}\right], \tag{1}$$

where ϵ_p is the permittivity of the prism. The angle required for resonance strongly depends on the change of ϵ_d, μ_d and the ϵ_m, μ_m, of the sensor materials as well as the probing samples, usually gas or liquid containing an agent that drives the change of refractive index, such as air and helium (in this case) or bio-samples in water. The MOSPR effect is an important parameter of a biosensor that can also be monitored to analyze probing samples on the sensor surface.

One of the most important parameters that affect the performance of MOSPR sensor is its sensitivity to the surrounding media that is a function of sample type or its concentration. Most MOSPR configurations record the phase, θ (in angular interrogation) or wavelength, λ (in wavelength interrogation) at a position where the derivative of the reflection curve is maximized. In most cases, the *Kretschmann* type configuration is preferred [4], and the same is used for sensitivity studies here. According to [13], the SPR sensitivity is defined as

$$S_{\text{SPR}} = \left(\frac{[R_{p(\text{air})} - R_{p(\text{helium})}]}{R_{p(\text{air})m}} \times 100\right) \Big/ \Delta n[\%/\text{RIU}] \tag{2}$$

and the MOSPR sensitivity is defined as

$$S_{\text{MOSOR}} = \left(\frac{[\Delta R_{p(\text{air})} - \Delta R_{p(\text{helium})}]}{\Delta R_{p(\text{air})m}} \times 100\right) \Big/ \Delta n[\%/\text{RIU}], \tag{3}$$

where $R_{p(\text{air})m}$ is the magnitude of the reflected intensity at an incident angle θ_m. The θ_m is the angle at which the first derivative $[(\delta R_{p(\theta)})/\delta\theta]$ is maximized, $\Delta R_{p(\text{air})}$ and $\Delta R_{p(\text{helium})}$ are the changes in the reflectivity due to modulating the H field for air and helium, respectively at θ_m. The difference $\Delta R_{p(\text{air})} - \Delta R_{p(\text{helium})}$ is normalized by $\Delta R_{p(\text{air})m}$, where $\Delta R_{p(\text{air})m}$ is the maximal for the first derivative $\delta(\Delta R_{p(\text{air})}\theta)/\Delta\theta_{(\text{air})}$. The Δn in (2) and (3) is the difference in the refractive indices between air and helium media, and RIU denotes refractive-index-unit here.

3 Results

Figure 2 shows normalized reflectivity, R_p and differential reflectivity, $\Delta R_p = [R_{p(H=0)} - R_{p(H=H)}]$ profiles for the Ti (2 nm)/Co (8 nm)/Au (50 nm) multilayer configuration (shown in fig. 1), with air and helium as probing media. These profiles were obtained with the p-polarized light at λ = 515, 532, and 632.8 nm for both fig. 2(a) air and fig. 2(b) helium media in the absence ($H = 0$) and presence ($H = H$) of applied transverse H field.

The resonance angle at which the coupling of the incident light and the surface plasmon waves occurs is media dependent, and it varies slightly at all the excitation wavelengths. As shown in figs. 2(a)–(c), no sharp change in the reflectivity is observed at or near the critical angle (a position of a minimum reflectivity) at the excitation wavelength, $\lambda = 515$ nm. No sharp reflectivity minima is observed even after extending the λ to 532 nm. However, the calculated reflectivity profiles showed a sharp dip in reflectivity at $\lambda = 632.8$ nm for both media. Figure 2(c) shows the R_p plotted against the incident angle, θ at $\lambda = 632.8$ nm, for the $H = 0$ and $H = H$ cases, and the inset in the top right shows an enlarged reflectivity view for clarity.

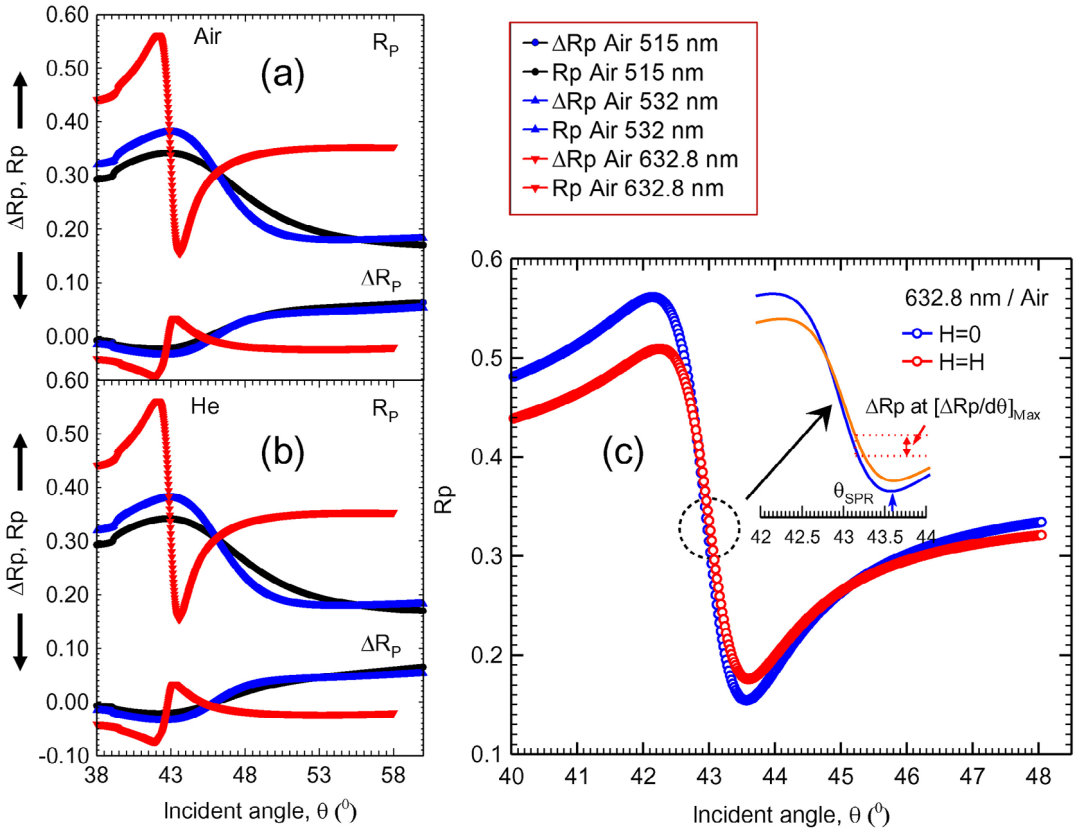

Fig. 2. Reflectivity (R_p) and differential reflectivity (ΔR_p) for (a) air and (b) helium media at $\lambda = 515$, 532, and 632.8 nm and (c) R_p plotted against the narrower range of an incident angle (40 to 48°) at $\lambda = 632.8$ nm, at $H = 0$ and $H = H$. The legend for (b) are the same as the legend shown for (a) in the top right of the figure with the air replaced by helium. The top right in the inset in (c) shows an enlarged view for clarity.

Figure 3(a) shows normalized SPR (SPR sensitivity) and MOSPR (MOSPR sensitivity) profiles calculated for the Ti (2 nm)/Co (8 nm)/Au (50 nm) multilayers with p-polarized incident light and transverse H field at $\lambda = 515$ nm for air-helium media. Both the SPR and MOSPR sensitivities, in this case, were calculated using the sensitivity metrics reported in (2) and (3). While the MOSPR sensitivity is drastically increased, the sensitivity profile is broad. Although no sharp peak is observed, the magnitude of MOSPR sensitivity in fig. 3(a) is still much larger than the magnitude of SPR sensitivity shown in figs. 2(a)–(c).

Figure 3(b) shows normalized SPR (SPR sensitivity) and MOSPR (MOSPR sensitivity) profiles calculated again, for the multilayers with p-polarized light and transverse H field at $\lambda = 632.8$ nm for air-helium media and at applied transverse H field. As shown, the MOSPR sensitivity in fig. 3(b) is increased by 12.5× under a similar resonance condition in fig. 3(a), and the MOSPR curves becomes sharper. In addition to this, the SPR sensitivity/figure of merit also improves (by almost 10×) as compared to the results obtained for the same configuration in fig. 3(a). This result provides important information about the excitation wavelength and sensitivity.

Figure 4 shows normalized SPR and MOSPR profiles calculated for the multilayers with $t_{\mathrm{Co}} = 4$ nm, for the p-polarized light at $\lambda = 632.8$ nm and at applied transverse H fields. Compared to the MOSPR sensitivity calculated for the multilayer with $t_{\mathrm{Co}} = 8$ nm in fig. 3(b), the MOSPR sensitivity is increased by over 3× in fig. 4. In addition to this, both the SPR and MOSPR curves becomes sharper. This result provides important information about the sensitivity of the MOSPR sensors that depends on the excitation wavelength of incident light, multilayer parameters (layer thicknesses), and excitation configuration. The performance parameters of SPR and MOSPR sensors for air-helium media are shown in table 2.

In addition to t_{Co}, the sharpness of the MOSPR spectra depends on the magnitude of the real and imaginary components of the dielectric constant. In the case where $\epsilon_r \gg 1$ and $\epsilon_r \gg \epsilon_i$, small damping occurs meaning sharper occurrence of the resonance curve (for more details, see [4]).

Ag (and Co/Ag) have high real to imaginary permittivity ratio (ϵ_r/ϵ_i) of ≈ 38 in the visible regime. In our previous works, Ag-based material demonstrated the largest SPR peak at resonance [13]. Compared to the Ag-based devices, Au and Co/Au based material have the smaller ϵ_r/ϵ_i of ≈ 7.33. Although the ϵ_r/ϵ_i of Au based materials is smaller and the SPR resonance peak is broader, Au-based biosensors are still being actively considered for biosensing and/or bioimaging as the detection can be achieved with high accuracy due to the high chemical stability possessed by these sensors.

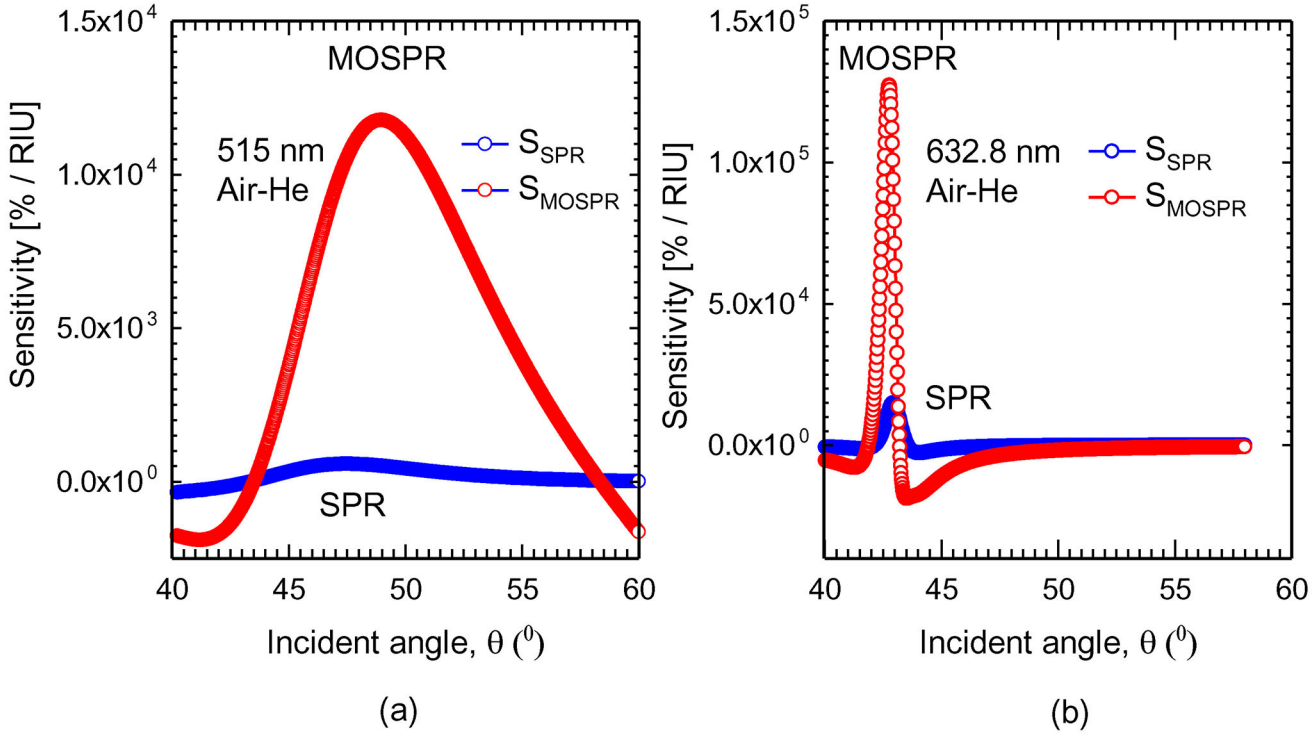

Fig. 3. Comparison of SPR and MOSPR activities: Sensitivities calculated as the incident angle of the optical radiation is changed from 40 to 60°, for the two types of excitation wavelengths: 515 nm and 632.8 nm and the Co layer thickness, $t_{Co} = 8$ nm.

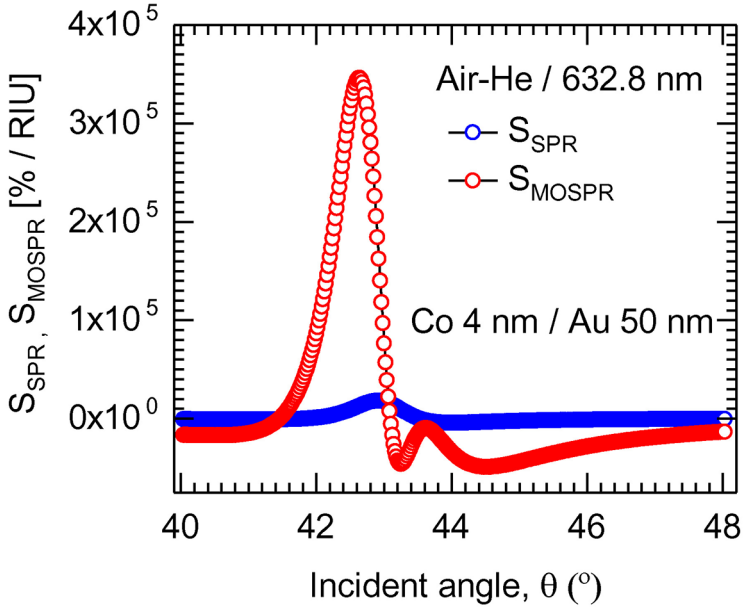

Fig. 4. Comparison of SPR and MOSPR sensitivities calculated at the excitation λ of 632.8 nm. The Co layer thickness, $t_{Co} = 4$ nm.

Table 2. Comparison of SPR (S_{SPR}) and MOSPR (S_{MOSPR}) sensitivities for air-helium media at $\lambda = 515$ nm and 632.8 nm, respectively.

Material (thickness)	λ (nm)	S_{SPR} (%/RIU)	S_{MOSPR} (%/RIU)
Co (8 nm)/Au (50 nm)	515	1.2×10^{03}	1.25×10^{04}
Co (8 nm)/Au (50 nm)	632.8	1.8×10^{04}	1.25×10^{05}
Co (4 nm)/Au (50 nm)	632.8	2.5×10^{04}	3.50×10^{05}

4 Conclusions

The SPR and magneto-optic SPR (MOSPR) sensitivity of magneto-plasmonic Co/Au multilayer-based sensors at three different operating wavelengths, λ, in the visible regime is studied here. The study shows that both the SPR and MOSPR sensitivities are strongly dependent on the excitation λ and Co layer thickness, t_{Co}. There is an enhancement in sensitivity of MOSPR configuration over SPR configuration for all λ in the visible regime. The SPR and MOSPR sensitivity also improved by 10× and 12.5×, respectively, when the λ is increased from 515 to 632.8 nm. The results suggested that the minimum reflectivity and peak positions and thus, the SPR and MOSPR effects significantly vary with excitation λ and sensor configurations, so the design optimization and analysis of the sensor configuration must be carried out meticulously. For example, the sensitivity of the MOSPR sensor increased by over 3× when the t_{Co} of the sensor configuration is optimized to 4 nm.

The sensitivity can be further improved by additional optimization of the material used for the sensor configuration. Overall, the present work opens the possibility of developing a MOSPR based practical bio-sensor with improved sensitivity without compromising the sensor performance. For example, the multilayer configuration studied in this work has the potential for applying in various industries, including but not limited to, medical diagnostics [21], biosensing [4], and surveying [14]. The sensing configuration used for gas media in this work can be extended to investigate the MOSPR effects in liquid media as well.

The work was supported by MITACS Canada (Grant # 4086) and Russian Foundation of Basic Research (Grants # 18-52-80038 and 18-52-45021).

References

1. C. Rizal, V. Belotelov, D. Ignatyeva, A.K. Zvezdin, S. Pisana, Condens. Matter **4**, 50 (2019).
2. C. Rizal, IEEE Trans. Magn. **54**, 10 (2018).
3. G. Pellegrini, G. Mattei, Plasmonics **9**, 6 (2014).
4. D.O. Ignatyeva, G.A. Knyazev, P.O. Kapralov, G. Dietler, S.K. Sekatskii, V.I. Belotelov, Sci. Rep. **6**, 28077 (2016).
5. E.A.F. Vila *et al.*, IEEE Trans. Magn. **44**, 11 (2008).
6. K. Lodewijks *et al.*, Nano Lett. **14**, 12 (2014).
7. C. Rizal, B. Niraula, H. Lee, J. Nanomed. Res. **3**, 3 (2016).
8. M. Fernández-Perea *et al.*, Phys. Rev. Lett. **111**, 027404 (2013).
9. C. Rizal, S. Pisana, I. Hrvoic, E. Fullerton, J. Phys. Commun. **2**, 2 (2018).
10. W.M. Robertson, E. Fullerton, J. Opt. Soc. Am. B **6**, 8 (1989).
11. A. Otto, Z. Phys. A **216**, 4 (1968).
12. K. Lin, Y. Lu, J. Chen, R. Zheng, P. Wang, H. Ming, Opt. Express **16**, 23 (2008).
13. C. Rizal, S. Pisana, I. Hrvoic, MDPI Biomed. Photon. Adv. **5**, 3 (2018).
14. C. Rizal, *Ferromagnetic Hybrid Nanostructure for Potential Clinical Applications: Theory, Design, Fabrication, Measurement, Data Analysis, & Characterization* (LAMBERT Academic Publishing GmbH & Co., 2018).
15. `http://www.schott.com`.
16. P. Johnson, R. Christy, Phys. Rev. B **9**, 12 (1974).
17. A.D. Rakić, A.B. Djurisić, J.M. Elazar, M.L. Majewski, Appl. Opt. **37**, 22 (1998).
18. J. González Díaz, B. Sepúlveda, A. GarcíaMartín, G. Armelles, Appl. Phys. Lett. **97**, 4 (2010).
19. C. Cuthbertson, M. Cuthbertson, Proc. R. Soc. London A **135**, 826 (1932).
20. P.E. Ciddor, Appl. Opt. **35**, 9 (1996).
21. K.-H. Yoon *et al.*, Investig. Radiol. **47**, 12 (2012).
22. M.H.H. Hasib, J.N. Nur, C. Rizal, K.N. Shushama, Condens. Matter **4**, 49 (2019).